

Article

Phase Transitions under the Electric Field in Ternary Ferroelectric Solid Solutions of $\text{Pb}(\text{In}_{1/2}\text{Nb}_{1/2})\text{O}_3$ – $\text{Pb}(\text{Mg}_{1/3}\text{Nb}_{2/3})\text{O}_3$ – PbTiO_3 near the Morphotropic Phase Boundary: Electric Approach

Makoto Iwata ^{1,*}, Soma Suzuki ¹, Yoshinori Takikawa ¹, Keiichiro Nakamura ² and Kazuhiko Echizenya ²

¹ Department of Physical Science and Engineering, Nagoya Institute of Technology, Nagoya 466-8555, Japan

² JFE Mineral & Alloy Company, Ltd., Chiba 260-0826, Japan

* Correspondence: miwata@nitech.ac.jp

Abstract: Temperature–field phase diagrams in the $[001]_c$ and $[011]_c$ directions in the cubic coordinate in 24% $\text{Pb}(\text{In}_{1/2}\text{Nb}_{1/2})\text{O}_3$ –46% $\text{Pb}(\text{Mg}_{1/3}\text{Nb}_{2/3})\text{O}_3$ –30% PbTiO_3 (24PIN–46PMN–30PT) and 31PIN–43PMN–26PT near the morphotropic phase boundary have been clarified by measuring the temperature dependences of permittivity under an electric field. Field-induced intermediate orthorhombic and tetragonal phases have been newly found in 24PIN–46PMN–30PT and 31PIN–43PMN–26PT, respectively. The temperature dependences of the remanent polarization have also been determined by polarization–electric field (P–E) hysteresis loop evaluation. On the basis of our experimental results, the phase transition and dielectric anisotropy in PIN–PMN–PT have been discussed.

Keywords: ferroelectric; relaxor; critical endpoint; electric field; morphotropic phase boundary



Citation: Iwata, M.; Suzuki, S.; Takikawa, Y.; Nakamura, K.; Echizenya, K. Phase Transitions under the Electric Field in Ternary Ferroelectric Solid Solutions of $\text{Pb}(\text{In}_{1/2}\text{Nb}_{1/2})\text{O}_3$ – $\text{Pb}(\text{Mg}_{1/3}\text{Nb}_{2/3})\text{O}_3$ – PbTiO_3 near the Morphotropic Phase Boundary: Electric Approach. *Crystals* **2024**, *14*, 121. <https://doi.org/10.3390/cryst14020121>

Academic Editors: Karuna Kara Mishra and Venkata Sreenivas Puli

Received: 26 December 2023

Revised: 18 January 2024

Accepted: 20 January 2024

Published: 26 January 2024



Copyright: © 2024 by the authors. Licensee MDPI, Basel, Switzerland. This article is an open access article distributed under the terms and conditions of the Creative Commons Attribution (CC BY) license (<https://creativecommons.org/licenses/by/4.0/>).

1. Introduction

Ternary ferroelectric solid solutions of $\text{Pb}(\text{In}_{1/2}\text{Nb}_{1/2})\text{O}_3$ – $\text{Pb}(\text{Mg}_{1/3}\text{Nb}_{2/3})\text{O}_3$ – PbTiO_3 (PIN–PMN–PT) belong to high-performance relaxor ferroelectrics [1,2], where PMN and PIN are relaxors [3], and PT is a typical displacive-type ferroelectric material. Among them, binary complex ferroelectric solid solutions of PMN– x PT and PIN– x PT show the morphotropic phase boundary (MPB) at $x = 30$ and 37% on temperature–concentration phase diagrams, respectively [4,5]. Generally, the colossal dielectric and piezoelectric responses in perovskite-type ferroelectrics appear near MPB. Indeed, PMN– x PT near MPB shows a significantly high electromechanical coupling coefficient, higher than 90% [2].

To understand such properties near MPB, a simple theoretical model based on the Landau–Devonshire free energy was reported, where the permittivity perpendicular to the spontaneous polarization becomes extremely high, since the anisotropy of the free energy becomes small in the parameter space [6]. A similar mechanism underlying such a giant response was also found in BaTiO_3 on the basis of the first principles studies [7]. In any case, it is certain that the anisotropic energy of the polarization near MPB in the relaxor ferroelectrics plays an essential role in their colossal dielectric and piezoelectric responses.

For PMN– x PT solid solution systems, the temperature–concentration phase diagram near MPB has been reported, where the rhombohedral, monoclinic, and tetragonal phases appear in ferroelectric phases [4,8]. An electromechanical coupling coefficient $k_{33}^* = 94\%$ was reported for PMN–33%PT, which is the highest reported among all piezoelectric materials [9]. However, the operating temperature range in PMN–33%PT is narrow, because the transition temperature between the tetragonal and rhombohedral phases is about 60 °C [4].

The temperature–field phase diagrams under various directions of an electric field in PMN– x PT were reported to clarify the average symmetry in the ferroelectric phase, where the ferroelectric critical endpoint (CEP) was found in the phase diagram [10–14]. On the basis of such temperature–field phase diagrams, we showed that relaxor ferroelectric

crystals almost behave similarly to a normal ferroelectric material under a DC biasing field [15]. Indeed, these field-induced phase transitions in the vicinity of MPB can be well reproduced on the basis of the Landau–Devonshire free energy [16]. The nonlinear dielectric susceptibility in PMN- x PT was also found to be well-analyzed within the Landau theory [17]. Recently, we have also found the aging effect on PMN- x PT [18].

On the other hand, in PIN, the chemical ordering of B-site cations (In and Nb) was clarified to be controlled by appropriate thermal treatment [19–22]. PIN crystals with different chemical orderings formed by different thermal treatments can be classified into three groups: the “ordered PIN”, “disordered PIN”, and “partly disordered PIN”. An as-grown single crystal is the partly disordered PIN, where the partly disordered PIN shows a broad peak of the dielectric constant without dielectric dispersion at about 90 °C [22].

For PIN- x PT solid solution systems, their temperature–concentration phase diagrams have been reported, where MPB between tetragonal and rhombohedral phases was found at about $x = 37\%$ near room temperature [5,23–26]. An electromechanical coupling coefficient in the rectangular bar mode $k_{33}' = 78\%$ was reported in PIN-37%PT [23]. The advantage of PIN-37%PT is that it has a wide operating temperature range ($T_c = 250$ °C) [22], although the electromechanical coupling coefficient in PIN-37%PT is smaller than that in PMN-33%PT [27].

Hosono et al. proposed the ternary ferroelectric solid solution system PIN–PMN–PT as a candidate material that realizes both a large electromechanical coupling coefficient (PMN–PT) and a high transition temperature (PIN–PT), and they reported that 16%PIN–51%PMN–33%PT (16PIN–51PMN–33PT) with a high transition temperature of 187 °C shows a large piezoelectric constant of 2200 pC/N [1]. To improve the performance of ternary ferroelectric solid solutions of PIN–PMN–PT, their physical properties with respect to the phase transition and MPB were extensively investigated using ceramic and single crystal samples of this system [28–35]. The temperature–field phase diagrams for 33PIN–35PMN–32PT and 23PIN–52PMN–25PT were studied to clarify the structural phase transition and stability of these materials under a biasing field [36–38]. A phenomenological approach to analyzing PIN–PMN–PT near MPB based on the Landau–Devonshire energy function with 10th-order terms in the polarization was discussed to explain qualitatively the engineered domain mechanism [39]. It seems that further experimental data are needed to determine the expansion coefficients taking into account the anisotropy of thermodynamic potential, which is the most important factor to explain the large dielectric and piezoelectric responses near MPB [6,7]. We pointed out in our previous paper that the data of a temperature–field phase diagram in various electric field directions are useful for evaluating the anisotropy [16].

Under these circumstances, in this paper, dielectric permittivities under the biasing field and the polarization–electric field (P–E) hysteresis loops in 24PIN–46PMN–30PT and 31PIN–43PMN–26PT near MPB were investigated. The temperature–field phase diagram in the $[001]_c$ and $[011]_c$ directions in the cubic coordinates and the spontaneous polarization as a function of temperature were clarified. On the basis of our experimental results, the phase transition and dielectric anisotropy in PIN–PMN–PT are discussed.

2. Experimental Procedure

Single crystal wafers in 24PIN–46PMN–30PT and 31PIN–43PMN–26PT near MPB were grown by the Bridgman technique [40]. Figure 1 shows the phase diagram of the ternary system of PIN–PMN–PT at room temperature, where 24PIN–46PMN–30PT and 31PIN–43PMN–26PT are shown by the solid and open circles, respectively. The straight dashed–dotted line connects the triple points in PIN–PT and PMN–PT, and the straight dotted line connects MPB at room temperature in PIN–PT and PMN–PT [4,5]. It is conjectured from Figure 1 that both materials are located near MPB and show phase sequences of cubic–rhombohedral and cubic–tetragonal–rhombohedral in 24PIN–46PMN–30PT and 31PIN–43PMN–26PT, respectively.

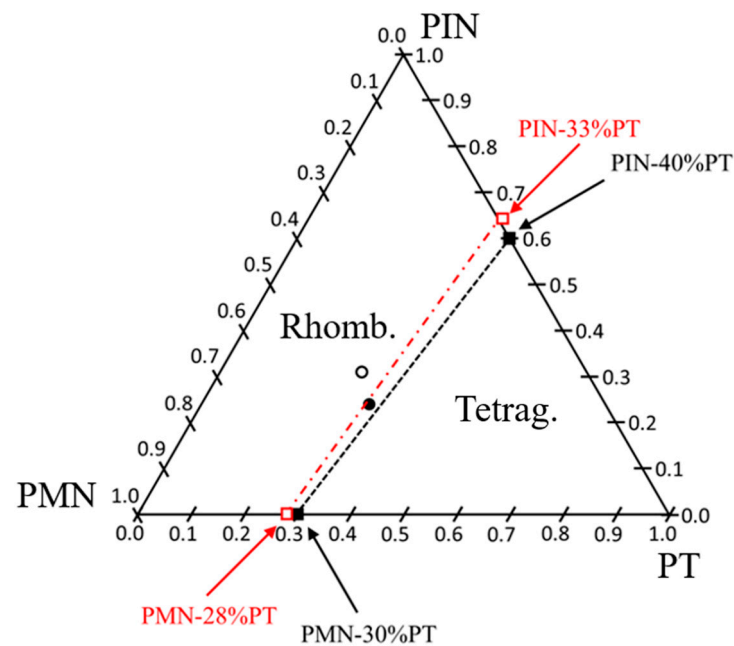


Figure 1. Ternary phase diagram for PIN–PMN–PT at room temperature, where 24PIN–46PMN–30PT and 31PIN–43PMN–26PT are shown by the solid and open circles, respectively. The straight dashed–dotted line connects with the triple points in PIN–PT and PMN–PT, and the straight dotted line connects with MPBs at room temperature in PIN–PT and PMN–PT.

Sample plates with thicknesses of about 250–500 μm were used in our experiments after annealing treatment for 3 h at 500 $^{\circ}\text{C}$. For the dielectric measurement, the parallel-plate capacitor of a sample with Au electrodes deposited on its face was prepared. Permittivity measurements under a DC biasing field were performed using an impedance/gain phase analyzer (NF ZGA5900) and a high-voltage amplifier (Trek 609E-6). In our measurement system, the AC probe voltage applied to measure dielectric permittivity is about 0.1–0.2 V, and the maximum DC biasing voltage applied to a sample during the measurement is about 800 V. Complex dielectric permittivity, $\varepsilon = \varepsilon' - i\varepsilon''$, was obtained in the range from 1 to 100 kHz after carefully removing the effects of the stray capacitance and residual impedance from the system.

A Sawyer–Tower circuit was used with a standard capacitor of 10 μF to evaluate P–E hysteresis loops, where a sinusoidal field in the frequency of 1 Hz and the amplitude of 14 kV/cm was applied to the sample. No correction of the phase lag using the phase compensation circuit was performed because of the low conductivity in 24PIN–46PMN–30PT and 31PIN–43PMN–26PT samples.

3. Results

3.1. Permittivity under Biasing Electric Field in 24PIN–46PMN–30PT

Figure 2a–c show typical examples of the temperature dependence of permittivity under the DC biasing fields of (a) 0, (b) 1.0, and (c) 2.0 kV/cm in the $[001]_c$ direction in 24PIN–46PMN–30PT. Three dielectric anomalies at T_m , T_{CT} , and T_{TR} are observed in each figure. It is seen that the temperatures T_{CT} and T_{TR} strongly depend on the electric field strength, and the temperature interval between T_{CT} and T_{TR} widens with increasing field strength along the $[001]_c$ direction, whereas the temperature T_m does not depend on the field strength within an experimental error. We conclude that T_{CT} and T_{TR} are the transition temperatures between the cubic and tetragonal phases and between the tetragonal and rhombohedral phases, respectively, whereas at least T_m does not indicate a ferroelectric phase transition. The details on T_m will be discussed in Section 4.1.

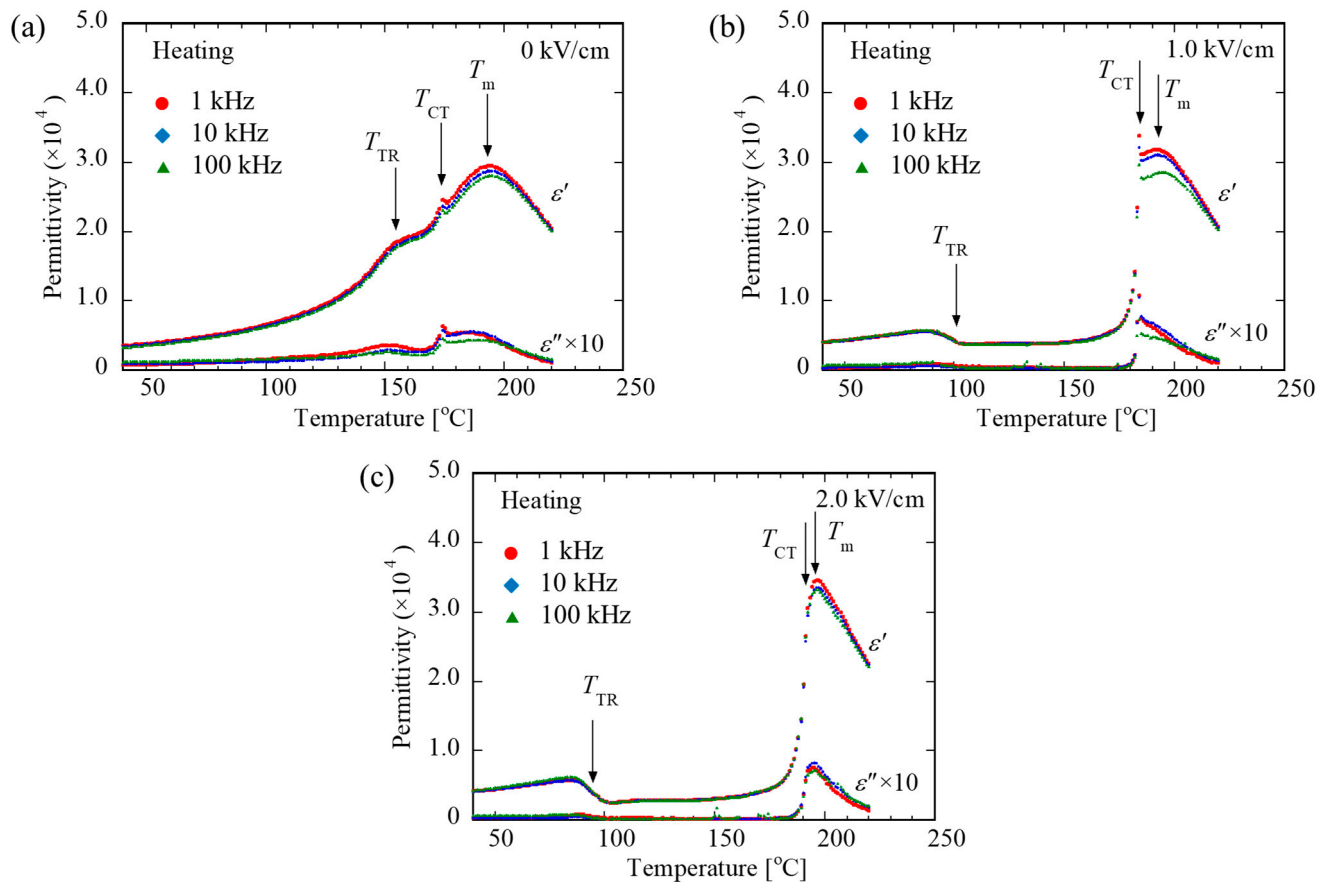


Figure 2. Typical examples of the permittivity as a function of temperature under the DC biasing fields of (a) 0, (b) 1.0, and (c) 2.0 kV/cm along the $[001]_c$ direction in 24PIN-46PMN-30PT. The temperatures T_{CT} , T_{TR} , and T_m are the phase transition temperatures between the cubic and tetragonal phases and between tetragonal and rhombohedral phases and the temperature showing a peak of permittivity (not ferroelectric transition temperature), respectively.

In Figure 3a–c, we also show typical examples of the temperature dependence of permittivity at 1 kHz under the DC biasing fields of (a) 0, (b) 2.0, and (c) 3.0 kV/cm along the $[011]_c$ direction in 24PIN-46PMN-30PT. At a permittivity along the $[011]_c$, three or four dielectric anomalies appear in each figure. All the temperatures showing the dielectric anomalies, except for T_m , depend on the electric field strength. We conclude that at least T_m does not indicate a ferroelectric phase transition. The subscripts of the temperatures indicating the dielectric anomalies and the assignment of the symmetry of the ferroelectric phases will be discussed in Section 4.1. The transition temperatures obtained from Figures 2a–c and 3a–c in 24PIN-46PMN-30PT are summarized in Table 1.

Figure 4a,b show the temperature–field phase diagrams along the $[001]_c$ and $[011]_c$ directions in 24PIN-46PMN-30PT, respectively. Circles and squares show the transition temperature determined from the permittivity measured on heating and cooling processes, respectively. The letters C, T, O, R, M_A , M_B , and M_C indicate cubic, tetragonal, orthorhombic, rhombohedral, monoclinic A, monoclinic B, and monoclinic C symmetries, respectively [8]. The letters in parentheses show the rigorous symmetry under the electric field along each direction. Experimental results for two samples are shown in Figure 4a,b to confirm sample dependence. It is seen that phase transition temperatures below 1 kV/cm are not consistent with those above 1 kV/cm owing to the relaxor nature of the diffuse phase transition. The assignment of the symmetry in the ferroelectric phases will be discussed in Section 4.1.

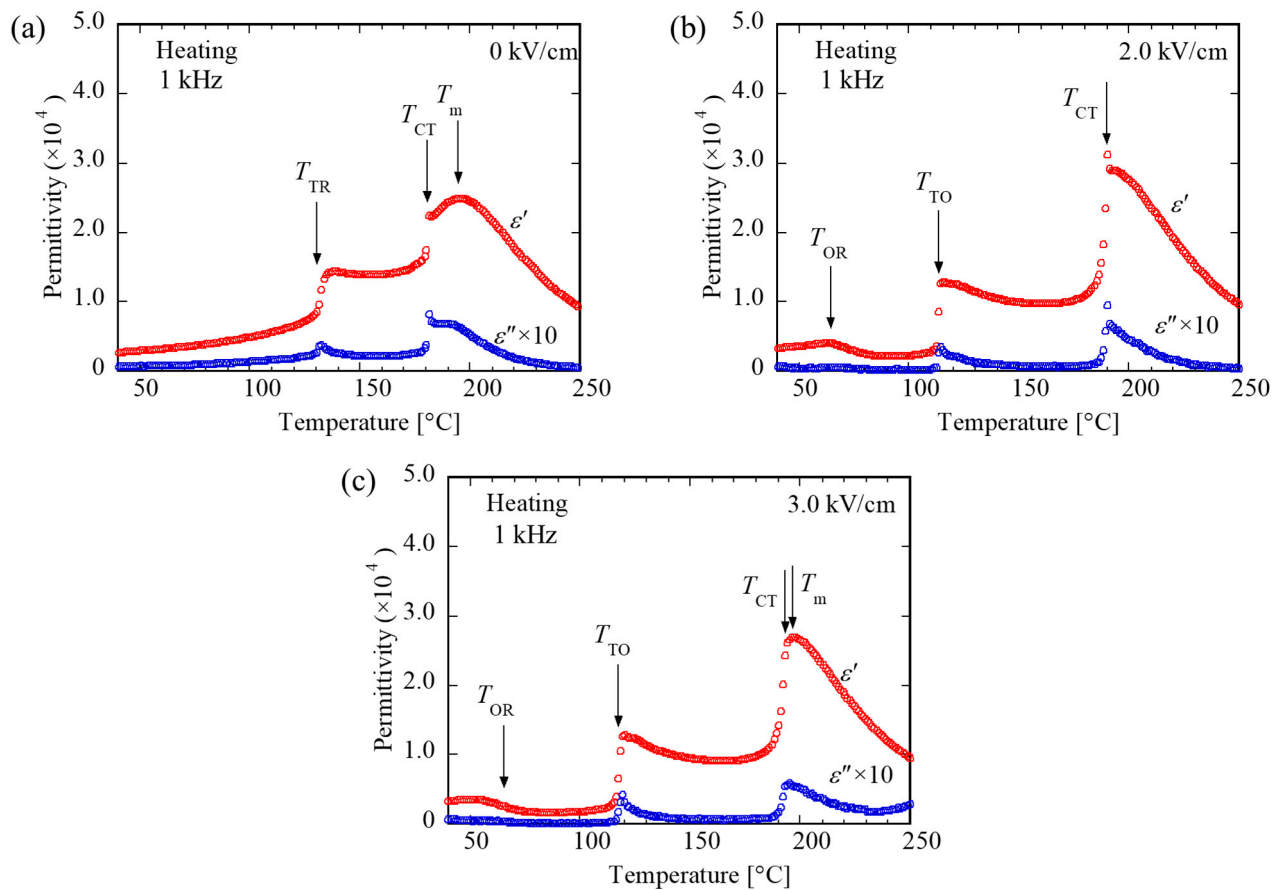


Figure 3. Typical examples of the temperature dependence of permittivity at 1 kHz under the DC biasing fields of (a) 0, (b) 2.0, and (c) 3.0 kV/cm along the $[011]_c$ direction in 24PIN-46PMN-30PT. The temperatures T_{CT} , T_{TO} , T_{OR} , and T_m are the phase transition temperatures between the cubic and tetragonal phases, between the tetragonal and orthorhombic phases, and between the orthorhombic and rhombohedral phases, and the temperature showing a peak of the permittivity (not ferroelectric transition temperature), respectively.

Table 1. Phase transition temperatures measured on heating in 24PIN-45PMN-30PT. T_m is determined from permittivity peak at 1 kHz.

DC Biasing Field [kV/cm] [001] Direction	T_m [°C]	T_{CT} [°C]	T_{TR} [°C]		
0	193	174	155		
1.0	193	184	101		
2.0	195	191	94		
DC Biasing Field [kV/cm] [011] Direction	T_m [°C]	T_{CT} [°C]	T_{TR} [°C]	TTO [°C]	TOR [°C]
0	195	181	131		
2.0	190			113	64
3.0	196	193		117	65

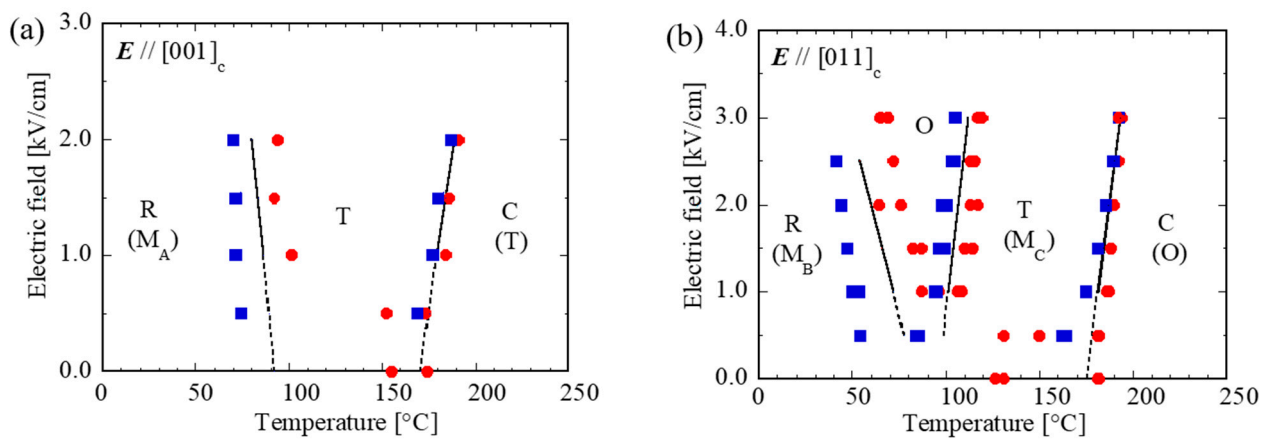


Figure 4. Temperature–field phase diagrams along (a) $[001]_c$ and (b) $[011]_c$ directions in 24PIN–46PMN–30PT. Circles and squares show transition temperatures determined from the permittivity measured during heating and cooling processes, respectively. Solid lines are the phase boundary, and dotted lines show the eye guide extrapolating the phase boundary. The letters C, T, O, R, M_A , M_B , and M_C indicate cubic, tetragonal, orthorhombic, rhombohedral, monoclinic A, monoclinic B, and monoclinic C symmetries, respectively [8]. The letters in the parentheses show the rigorous symmetries under the electric field along each direction.

3.2. Permittivity under Biasing Electric Field in 31PIN–43PMN–26PT

The temperature dependences of permittivity under the DC biasing fields of 0, 1.0, and 2.0 kV/cm along the $[001]_c$ direction in 31PIN–43PMN–26PT are respectively shown in Figure 5a–c as typical examples. It is seen that only the temperature T_m showing the maximum permittivity is found in Figure 5a, whereas three dielectric anomalies at T_m , T_{CT} , and T_{TR} appear in Figure 5b,c. The temperatures T_{CT} and T_{TR} strongly depend on the electric field strength, and the temperature interval between T_{CT} and T_{TR} widens with increasing field strength, whereas the temperature T_m does not depend on the field strength within an experimental error. Consequently, T_{CT} and T_{TR} are determined to be the transition temperatures between the cubic and tetragonal phases and between the tetragonal and rhombohedral phases, respectively, and T_m does not indicate a ferroelectric phase transition.

Figure 6a–c also show typical examples of the temperature dependence of permittivity at 1 kHz under the DC biasing field of (a) 0, (b) 1.0, and (c) 2.0 kV/cm along the $[011]_c$ direction in 31PIN–43PMN–26PT. One or two dielectric anomalies appear in each figure along the $[011]_c$ direction. The temperature T_{CR} depends on the electric field strength, whereas the temperature T_m does not within an experimental error. We conclude that T_{CR} is the transition temperature from cubic to rhombohedral phases, and at least T_m does not indicate a ferroelectric phase transition. The transition temperatures obtained from Figures 5a–c and 6a–c in 31PIN–43PMN–26PT are summarized in Table 2.

Figure 7a,b show the temperature–field phase diagrams along the $[001]_c$ and $[011]_c$ directions in 31PIN–43PMN–26PT, respectively. Circles and squares show the transition temperatures determined from the permittivity measured during the heating and cooling processes, respectively. The letters C, T, O, R, M_A , and M_B indicate cubic, tetragonal, orthorhombic, rhombohedral, monoclinic A, and monoclinic B symmetries, respectively [8]. The letters in parentheses show the rigorous symmetry under the electric field along each direction. To confirm sample dependence, the results of the transition temperature for two samples are shown in Figure 7b. It is seen that phase transition temperatures below 1 kV/cm are not consistent with those above 1 kV/cm owing to the relaxor nature of the diffuse phase transition. The assignment of the symmetry in the ferroelectric phases will be discussed in Section 4.1.

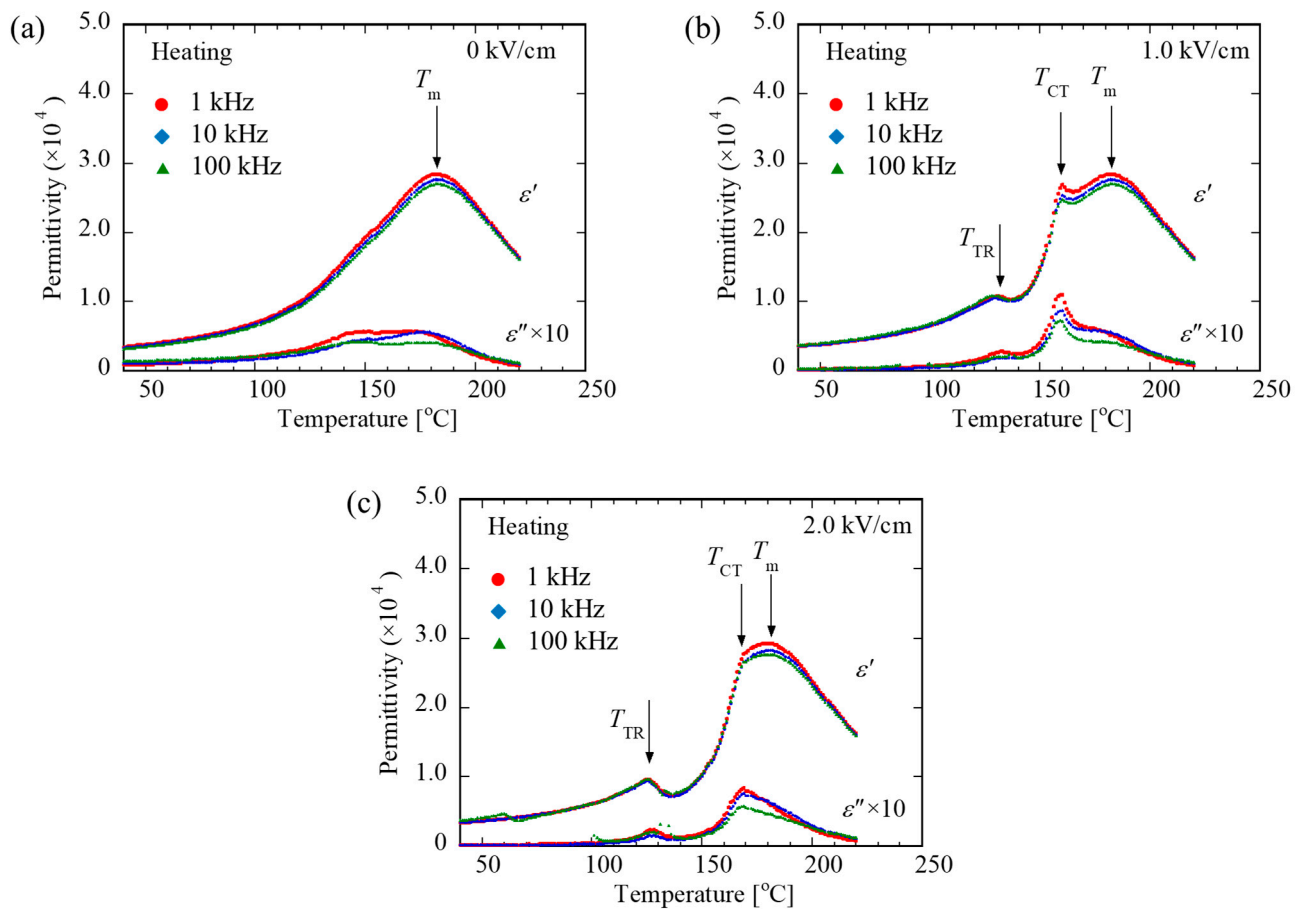


Figure 5. Typical examples of the temperature dependence of permittivity under the DC biasing fields of (a) 0, (b) 1.0, and (c) 2.0 kV/cm along the $[001]_c$ direction in 31PIN-43PMN-26PT. The temperatures T_{CT} , T_{TR} , and T_m are the phase transition temperatures between the cubic and tetragonal phases and between the tetragonal and rhombohedral phases and the temperature showing a peak of the permittivity (not ferroelectric transition temperature), respectively.

Table 2. Phase transition temperatures measured on heating in 31PIN-45PMN-30PT. T_m is determined from permittivity peak at 1 kHz.

DC Biasing Field [kV/cm] [001] Direction	T_m [°C]	T_{CT} [°C]	T_{TR} [°C]
0	182		
1.0	182	160	134
2.0	181	168	126
DC Biasing Field [kV/cm] [011] Direction	T_m [°C]	T_{CT} [°C]	T_{TR} [°C]
0	178		
2.0	178	148	
3.0	178	156	

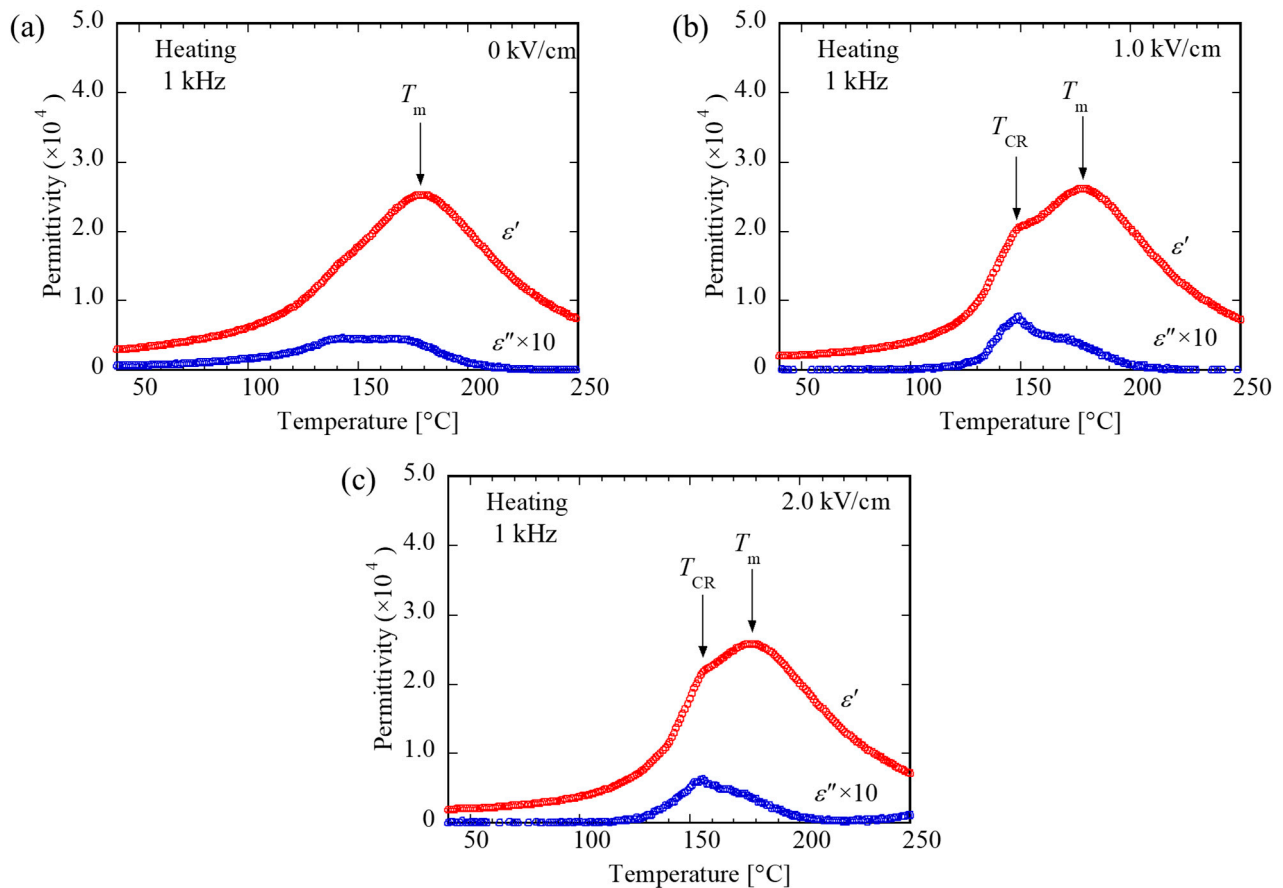


Figure 6. Typical examples of the temperature dependence of permittivity at 1 kHz under the DC biasing fields of (a) 0, (b) 1.0, and (c) 2.0 kV/cm along the $[011]_c$ direction in 31PIN-43PMN-26PT. The temperatures T_{CR} and T_m are the phase transition temperature between the cubic and rhombohedral phases and the temperature showing a peak of the permittivity (not ferroelectric transition temperature), respectively.

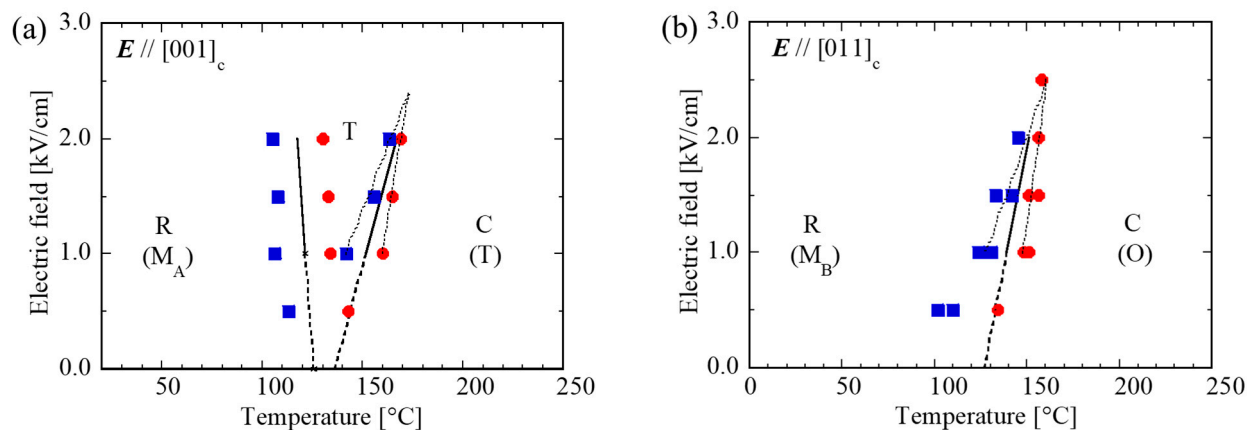


Figure 7. Temperature-field phase diagrams along (a) $[001]_c$ and (b) $[011]_c$ directions in 31PIN-43PMN-26PT. Circles and squares show transition temperatures determined from the permittivity measured during heating and cooling processes, respectively. Solid lines are the phase boundary, and dotted lines show the eye guide extrapolating the phase boundary. The letters C, T, O, R, M_A , and M_B indicate cubic, tetragonal, orthorhombic, rhombohedral, monoclinic A, and monoclinic B symmetries, respectively [8]. The letters in the parentheses show the rigorous symmetries under the electric field along each direction.

3.3. P–E Hysteresis Loops

Figure 8a–d show typical examples of the P–E hysteresis loops in different electric fields along the $[001]_c$ direction in 24PIN–46PMN–30PT, where the frequency of the electric fields is 1 Hz. The P–E hysteresis loops were measured in the temperature range from 180 to 30 °C during the cooling process. It is considered that in Figure 8a, the imperfect triple-loop pattern basically indicates the field-induced transition in the paraelectric phase. Figure 8b–d show typical P–E hysteresis loops revealing the polarization reversal in the ferroelectric phase.

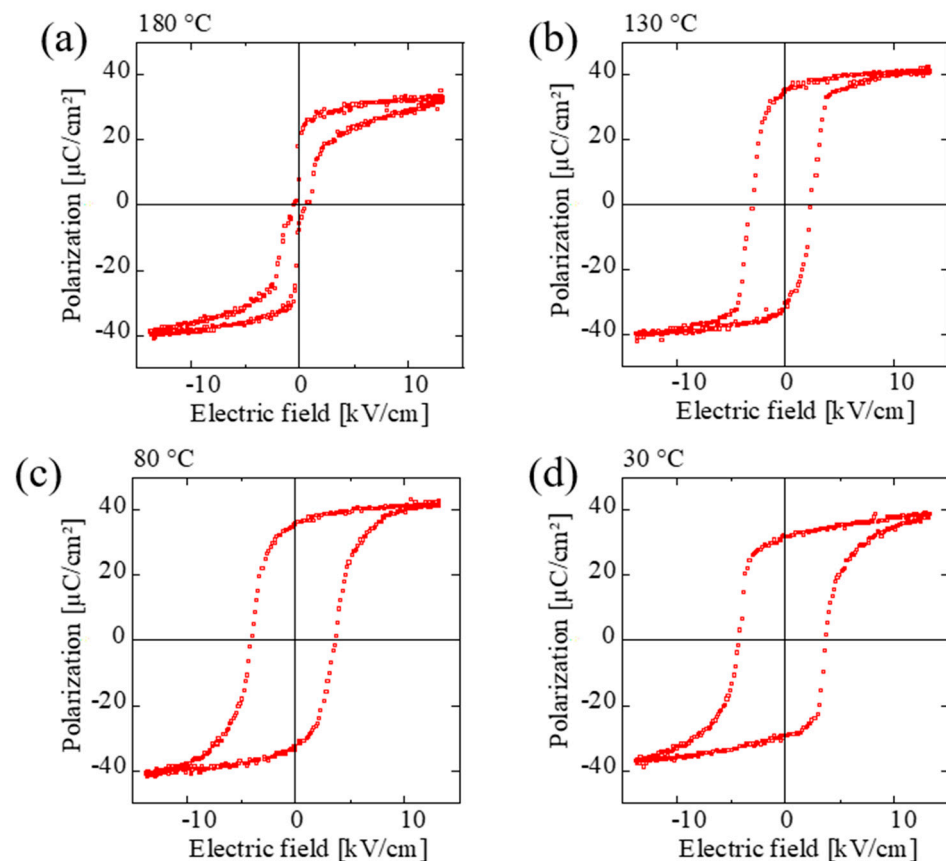


Figure 8. P–E hysteresis loops along the $[001]_c$ direction in 24PIN–46PMN–30PT. The frequency of the electric field applied is 1 Hz. The measurement temperatures are (a) 180 °C, (b) 130 °C, (c) 80 °C, and (d) 30 °C.

Typical examples of the P–E hysteresis loops in 31PIN–43PMN–26PT under different electric fields along the $[001]_c$ direction are shown in Figure 10a–d, where the frequency of the electric fields is 1 Hz, and the temperature range measured is from 180 to 30 °C during the cooling process. It is guessed that in Figure 10a, the imperfect triple-loop pattern basically indicates the field-induced transition in the paraelectric phase. Figure 10b–d show typical P–E hysteresis loops revealing the polarization reversal in the ferroelectric phase.

The temperature dependence of remanent polarization determined by the P–E hysteresis loop measurement is shown in Figure 9. The dotted lines indicate the transition temperature determined from Figure 4a, where $T_{CT} = 171$ °C and $T_{TR} = 92$ °C (see Section 3.1). At the transition temperature between the tetragonal and rhombohedral phases, an anomaly of the remanent polarization is found, although no jump of the polarization appears. This implies the coexistence of the tetragonal, orthorhombic, and rhombohedral phases.

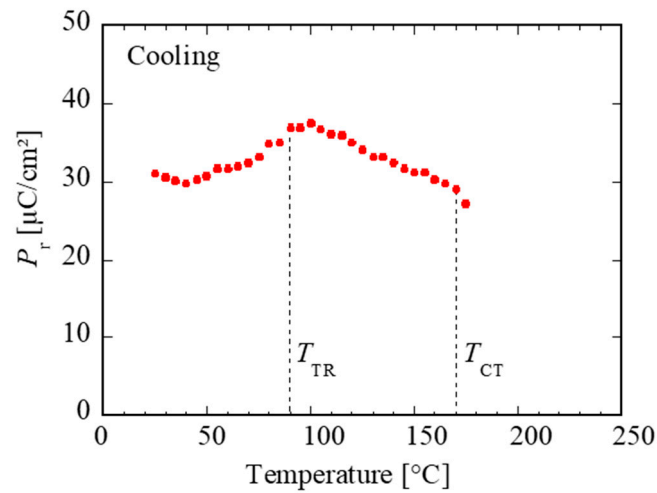


Figure 9. Temperature dependence of the remanent polarization component along the $[001]_c$ direction in 24PIN-46PMN-30PT.

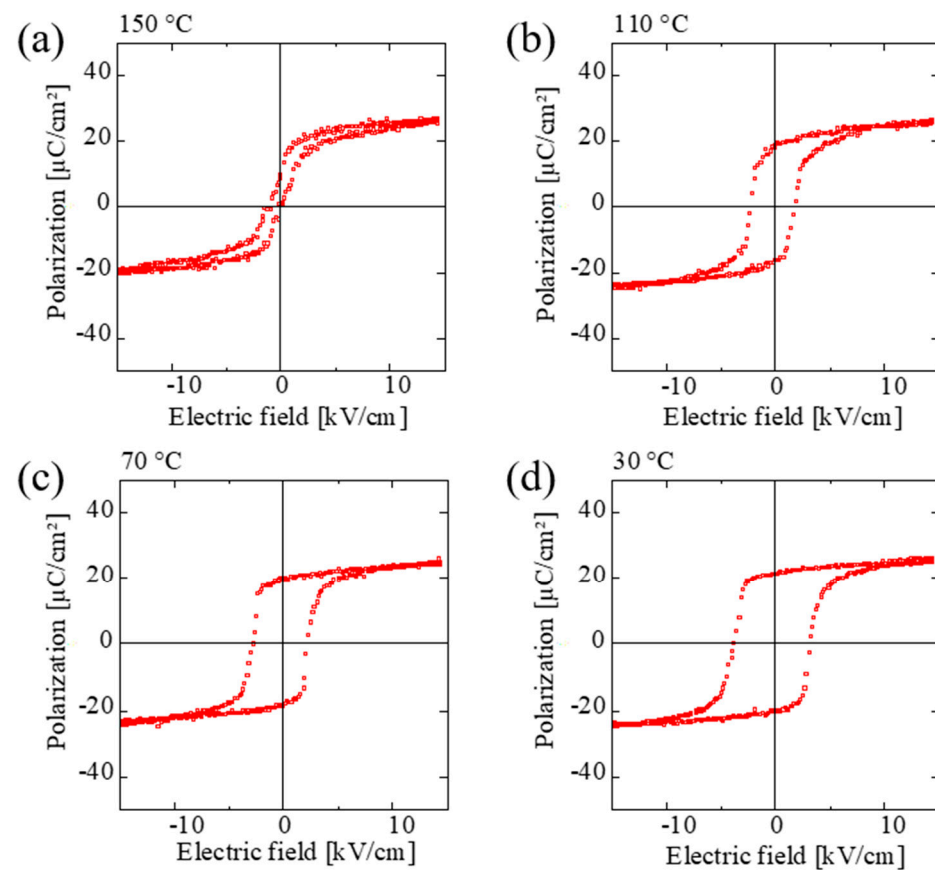


Figure 10. P-E hysteresis loops along the $[001]_c$ direction in 31PIN-43PMN-26PT. The frequency of the electric field applied is 1 Hz. The measurement temperatures are (a) 150 °C, (b) 110 °C, (c) 70 °C, and (d) 30 °C.

Figure 11 shows the temperature dependence of the remanent polarization obtained by the P-E hysteresis loop measurement, where the dotted line indicates the transition temperature determined from Figure 7b, where $T_{CR} = 127$ °C (see Section 3.2). Note that in Figure 11, the true polarization value in the rhombohedral phase must be multiplied by $\sqrt{3}$.

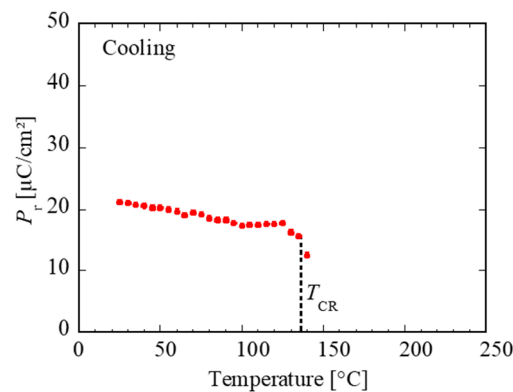


Figure 11. (Color online) Temperature dependence of the remanent polarization component along the $[001]_c$ direction in 31PIN-43PMN-26PT.

4. Discussion

4.1. Assignment of the Symmetry in 24PIN-46PMN-30PT

Let us start with the assignment of the ferroelectric phase in the phase diagram along the $[001]_c$ direction in 24PIN-46PMN-30PT. It is seen in Figure 4a that the temperature interval of the tetragonal phase extends as the electric field along the $[001]_c$ direction increases, which is consistent with the stability of the polarization in the tetragonal phase under the field in the $[001]_c$ direction. Therefore, by extrapolating the phase boundary from the electric field above 1 kV/cm to zero field, we conclude that the phase transition sequence under zero biasing field is determined to be the C–T–R phases. The phase transitions at T_{CT} and T_{TR} under zero biasing field are of the first order, and the transition temperatures are at $T_{CT} = 171$ °C and $T_{TR} = 92$ °C. We were unable to determine CEP in the C–T phase transition because of the diffuseness of this phase transition. By extrapolating the phase boundary above 1 kV/cm to $E = 0$, we also estimated the slopes of the C–T and T–R phase boundaries to be $dE/dT_{CT}|_{E=0} = 0.11$ kV/cmK and $dE/dT_{TR}|_{E=0} = -0.16$ kV/cmK under an electric field along the $[001]_c$ direction, respectively.

Next, we assign the ferroelectric phases in the phase diagram along the $[011]_c$ direction shown in Figure 4b. The temperature interval of the orthorhombic phase extends as the electric field along the $[011]_c$ direction increases, which is consistent with the stability of the polarization in the orthorhombic phase under the field in the $[011]_c$ direction. We conclude that the orthorhombic phase appears only under the field along the $[011]_c$ direction. The field-induced orthorhombic phase is determined to be a metastable phase under zero biasing field, because no orthorhombic phase appears in the electric field along the $[001]_c$ direction.

The transition temperature T_{CT} is determined to be 175 °C by extrapolating the phase boundary from the electric field above 1 kV/cm to zero field. The slope of the C–T phase boundary is obtained to be $dE/dT_{CT}|_{E=0} = 0.17$ kV/cmK under the electric field along the $[011]_c$ direction. The reason for the difference of 4 °C in the phase transition temperature T_{CT} along the $[001]_c$ and $[011]_c$ directions is guessed to be the sample dependence.

In general, the ferroelectric transition temperature depends on the direction and strength of the biasing field, because the electric field is the conjugate force to the polarization. Indeed, T_{CT} and T_{TR} were confirmed to depend on the biasing field, as shown in Figure 4a,b. However, T_m does not completely depend on the electric field within an experimental error. We considered that at least the temperature T_m at which the permittivity is maximum is not a ferroelectric transition temperature.

4.2. Assignment of the Symmetry in 31PIN-43PMN-26PT

Let us assign the ferroelectric phases in the phase diagram along the $[001]_c$ direction in 31PIN-43PMN-26PT. In Figure 7a, the temperature interval of the tetragonal phase extends with increasing electric field along the $[001]_c$ direction, which is consistent with the stability

of the polarization in the tetragonal phase under the field along the $[001]_c$ direction. The intermediate ferroelectric phase newly found is determined to be the tetragonal phase. With respect to the C–T phase transition, we find that the thermal hysteresis of the transition temperature decreases with increasing electric field. By extrapolating with straight lines (thin dotted line in Figure 7a), the critical endpoint is determined to be 173 °C and 2.4 kV/cm.

By extrapolating the phase boundary from the field above 1 kV/cm to zero field, we determined the transition temperatures to be $T_{CT} = 136$ °C and $T_{TR} = 126$ °C, and estimated the slopes of the boundaries C–T and T–R to be $dE/dT_{CT}|_{E=0} = 6.5 \times 10^{-2}$ kV/cmK and $dE/dT_{TR}|_{E=0} = -0.24$ kV/cmK in the electric field along the $[001]_c$ direction, respectively.

In the phase diagram only along the $[001]_c$ direction shown in Figure 7a, we were unable to determine whether a stable tetragonal phase exists under zero electric field. In the phase diagram along the $[011]_c$ direction shown in Figure 7b, no intermediate tetragonal phase was found. This indicates that the tetragonal phase is not stable under zero electric field. As for the C–T phase transition, it is found that the thermal hysteresis of the transition temperature decreases as the electric field increases. By extrapolating with straight lines (thin dotted line in Figure 7b, the temperature at which the phase transition changes from first to second order is determined to be 160 °C and 2.5 kV/cm, indicating the tricritical point. Dul'kin et al. showed the existence of a tricritical point in the C–R phase transition of 26PIN–46PMN–28PT with different compositions under an electric field along $[011]_c$ direction [35]. From the point of view of symmetry, these are presumed to be critical points of the same kind. Further detailed study of such tricritical points is needed.

By extrapolating the phase boundary above 1 kV/cm to $E = 0$, we determined the transition temperature T_{CR} to be 127 °C, and the slope of the C–R phase boundary is obtained to be $dE/dT_{CR}|_{E=0} = 8.3 \times 10^{-2}$ kV/cmK in the electric field along the $[011]_c$ direction. From the above, we conclude that the phase transition sequence under zero biasing field is considered to be the C–R phases, and the tetragonal phase is a metastable phase under zero biasing field.

4.3. Evaluation of the Phase Boundary Based on the Clausius–Clapeyron Equation

Let us focus on the slope of the phase boundary in the temperature–field phase diagram of the perovskite-type ferroelectrics on the basis of the Clausius–Clapeyron equation. We start with the Landau–Ginzburg–Devonshire free energy function f expressed in terms of the polarization components p_i ($i = 1-3$) as

$$f = \frac{\alpha}{2}(p_1^2 + p_2^2 + p_3^2) + \frac{\beta_1}{4}(p_1^4 + p_2^4 + p_3^4) + \frac{\gamma_1}{6}(p_1^6 + p_2^6 + p_3^6) + \frac{\gamma_2}{2}[p_1^4(p_2^2 + p_3^2) + p_2^4(p_3^2 + p_1^2) + p_3^4(p_1^2 + p_2^2)] + \frac{\gamma_3}{2}p_1^2p_2^2p_3^2 - \mathbf{p} \cdot \mathbf{E}, \quad (1)$$

where α is temperature-dependent, as shown by $\alpha = a(T - T_0)$, $a > 0$, $T_0 > 0$. The parameters β_1 , β_2 , γ_1 , γ_2 , and γ_3 are constants, $\mathbf{E} = (E_1, E_2, E_3)$ is the external electric field, and $\mathbf{p} = (p_1, p_2, p_3)$ the polarization. We truncated the free energy function at the sixth order of the polarization for simplicity. At this truncated free energy, the cubic (C), tetragonal (T), orthorhombic (O), and rhombohedral (R) phases are stable under zero external field, where the stable spontaneous polarizations in the C, T, O, R phases are defined as $(0, 0, 0)$, $(0, 0, p)$, $(0, q, q)$, and (r, r, r) , respectively.

We consider the slope of the boundary between the A and B phases at zero field in the temperature–field phase diagram based on the free energy in Equation (1), where the A and B phases are the C, T, O, and R phases. According to the Clausius–Clapeyron equation, the slope of the phase boundary is obtained as [41]

$$\frac{dE}{dT_c} = \frac{-a(\mathbf{p}_A^2 - \mathbf{p}_B^2)}{2(\mathbf{p}_B - \mathbf{p}_A) \cdot \mathbf{e}_E} = \frac{-\Delta S}{\Delta \mathbf{p} \cdot \mathbf{e}_E} \quad (2)$$

where e_E is the directional vector of the electric field $E/|E|$, and $\Delta p = p_B - p_A$ and $\Delta S = S_B - S_A = -a(p_B^2 - p_A^2)/2$ are the jumps of the polarization and the entropy at the phase boundary between the A and B phases, respectively. The derivation of the extended Clausius-Clapeyron equation in ferroelectrics is given in Appendix A. All the slopes of the phase boundary at zero field in the temperature–field phase diagram are summarized in Table 3. The slope of the phase boundary can be determined if the polarizations at the phase boundary in the A and B phases are known. Note that the Clausius-Clapeyron equation presented in Equation (2) is also applicable to the free energy expanded to the 10th-order term of the polarization recently proposed by Lv et al. [39].

Table 3. Slope of the phase boundary between A and B phases at zero electric field in the temperature–field phase diagram. $\Delta p = p_B - p_A$ and $\Delta S = S_B - S_A$.

A-B Transition	p_A	p_B	$\frac{dE}{dT_c} = -\frac{\Delta S}{\Delta p \cdot e_E}$		
			$e_E = \begin{pmatrix} 0 \\ 0 \\ 1 \end{pmatrix}$	$e_E = \frac{1}{\sqrt{2}} \begin{pmatrix} 0 \\ 1 \\ 1 \end{pmatrix}$	$e_E = \frac{1}{\sqrt{3}} \begin{pmatrix} 1 \\ 1 \\ 1 \end{pmatrix}$
C–T	$\begin{pmatrix} 0 \\ 0 \\ 0 \end{pmatrix}$	$\begin{pmatrix} 0 \\ 0 \\ p \end{pmatrix}$	$\frac{ap}{2}$	$\frac{\sqrt{2}ap}{2}$	$\frac{\sqrt{3}ap}{2}$
C–O	$\begin{pmatrix} 0 \\ 0 \\ 0 \end{pmatrix}$	$\begin{pmatrix} 0 \\ q \\ q \end{pmatrix}$	aq	$\frac{\sqrt{2}aq}{2}$	$\frac{\sqrt{3}aq}{2}$
C–R	$\begin{pmatrix} 0 \\ 0 \\ 0 \end{pmatrix}$	$\begin{pmatrix} r \\ r \\ r \end{pmatrix}$	$\frac{3ar}{2}$	$\frac{3\sqrt{2}ar}{4}$	$\frac{\sqrt{3}ar}{2}$
T–O	$\begin{pmatrix} 0 \\ 0 \\ p \end{pmatrix}$	$\begin{pmatrix} 0 \\ q \\ q \end{pmatrix}$	$\frac{a(2q^2 - p^2)}{2(q - p)}$	$\frac{\sqrt{2}a(2q^2 - p^2)}{2(2q - p)}$	$\frac{\sqrt{3}a(2q^2 - p^2)}{2(2q - p)}$
T–R	$\begin{pmatrix} 0 \\ 0 \\ p \end{pmatrix}$	$\begin{pmatrix} r \\ r \\ r \end{pmatrix}$	$\frac{a(3r^2 - p^2)}{2(r - p)}$	$\frac{\sqrt{2}a(3r^2 - p^2)}{2(2r - p)}$	$\frac{\sqrt{3}a(3r^2 - p^2)}{2(3r - p)}$
O–R	$\begin{pmatrix} 0 \\ q \\ q \end{pmatrix}$	$\begin{pmatrix} r \\ r \\ r \end{pmatrix}$	$\frac{a(3r^2 - 2q^2)}{2(r - q)}$	$\frac{\sqrt{2}a(3r^2 - 2q^2)}{4(r - q)}$	$\frac{\sqrt{3}a(3r^2 - 2q^2)}{2(3r - 2q)}$

Since no jump of the spontaneous polarization at the transition point can be observed in our experimental result, we only evaluate the slope of the boundary between the cubic and tetragonal phases in 24PIN–46PMN–30PT, where the slopes of the C–T boundaries along the $[001]_c$ and $[011]_c$ directions are 0.11 and 0.17 kV/cmK, respectively. From Table 3, the ratio of the slopes is $\sqrt{2}$. It is seen that the ratio 0.17/0.11 is $1.5 \cong \sqrt{2}$ within an experimental error, which is consistent with our experimental results.

5. Conclusions

In this study, we have clarified the temperature–field phase diagrams along the $[001]_c$ and $[011]_c$ directions in the cubic coordinate in 24PIN–46PMN–30PT and 31PIN–43PMN–26PT near MPB. The temperature dependences of the remanent polarization have also been determined by P–E hysteresis loop observation.

In 24PIN–46PMN–30PT, we conclude that the phase transition sequence without an external field is the C–T–R phases, where the phase transition temperatures are 171 and 92 °C. The field-induced transition to the ferroelectric orthorhombic phase appears only under the electric field along the $[011]_c$ direction. This indicates that the orthorhombic phase observed in the electric field is a metastable phase under zero field. We analyzed the slope of the phase boundary at zero field in the temperature–field phase diagram on the

basis of the Clausius–Clapeyron equation, and consequently, we confirmed that the phase diagrams along the $[001]_c$ and $[011]_c$ directions are consistent within an experimental error.

In 31PIN–43PMN–26PT, the phase transition sequence without an external field is the C–R phases, as determined by extrapolating the phase boundary above 1 kV/cm to $E = 0$, where the transition temperature is 127 °C. The field-induced transition to the tetragonal phase appears only under the electric field along the $[001]_c$ direction, indicating a metastable phase under zero field.

We experimentally found that many ferroelectric phases including metastable orthorhombic and tetragonal phases exist in PIN–PMN–PT. This implies that the local minima of the free energy as a function of polarization in various directions compete with each other, and then the anisotropy of the Landau–Ginzburg–Devonshire free energy in the polarization space is small. Therefore, we conclude that the large dielectric and piezoelectric responses in these materials near MPB come from the transversal instability [6]. Further investigations from the viewpoint of the anisotropy in the thermodynamic potential are required to clarify the physical properties in PIN–PMN–PT solid solution systems.

Author Contributions: Conceptualization, M.I.; crystal growth, K.N. and K.E.; investigation, M.I., S.S. and Y.T. All authors have read and agreed to the published version of the manuscript.

Funding: This research was funded in part by a Grant-in-Aid for Scientific Research (B) (No. 22H01774) from the Japan Society for the Promotion of Science for M.I.

Data Availability Statement: No new data were created or analyzed in this study. Data sharing is not applicable to this article.

Acknowledgments: We would like to thank Keigo Yamashita for his technical assistance.

Conflicts of Interest: Author Keiichiro Nakamura and Kazuhiko Echizenya were employed by the company JFE Mineral & Alloy Company Ltd. The remaining authors declare that the research was conducted in the absence of any commercial or financial relationships that could be construed as a potential conflict of interest.

Appendix A

We derive the extended Clausius–Clapeyron equation shown in Equation (1). Let G_I and G_{II} be the Gibbs free energy densities at the phase boundary between phase I and phase II, respectively, where the Gibbs free energy density is a function of temperature T , and electric field E . The total derivative of G can be written as

$$dG = -SdT - p \cdot dE, \quad (A1)$$

where S is the entropy, and p is the polarization. From the condition $dG_I = dG_{II}$ at the boundary ($T = T_c$), we can write

$$-S_I dT_c - p_I \cdot dE = -S_{II} dT_c - p_{II} \cdot dE, \quad (A2)$$

and then

$$\Delta S dT_c + \Delta p \cdot E = 0, \quad (A3)$$

where $\Delta S = S_{II} - S_I$ and $\Delta p = p_{II} - p_I$. The extended Clausius–Clapeyron equation is obtained as

$$\frac{dE}{dT_c} = \frac{-\Delta S}{\Delta p \cdot e_E} \quad (A4)$$

where $E = |E|$ and $e_E = E/|E|$.

References

- Hosono, Y.; Yamashita, Y.; Sakamoto, H.; Ichinose, N. Large Piezoelectric Constant of High-Curie-Temperature $\text{Pb}(\text{In}_{1/2}\text{Nb}_{1/2})\text{O}_3$ - $\text{Pb}(\text{Mg}_{1/3}\text{Nb}_{2/3})$ - PbTiO_3 Ternary Single Crystal near Morphotropic Phase Boundary. *Jpn. J. Appl. Phys.* **2002**, *41*, L1240–L1242. [\[CrossRef\]](#)
- Zhang, S.; Li, F. High performance ferroelectric relaxor- PbTiO_3 single crystals: Status and perspective. *J. Appl. Phys.* **2012**, *111*, 031301. [\[CrossRef\]](#)
- Samara, G.A. Advances in Research and Applications. In *Solid State Physics*; Ehrenreich, H., Spaepen, F., Eds.; Academic Press: New York, NY, USA, 2001; Volume 56, p. 239.
- Shrout, T.R.; Chang, Z.P.; Kim, N.; Markgraf, S. Dielectric behavior of single crystals near the $(1-x)\text{Pb}(\text{Mg}_{1/3}\text{Nb}_{2/3})\text{O}_3$ -(x) PbTiO_3 morphotropic phase boundary. *Ferroelectr. Lett. Sect.* **1990**, *12*, 63–69. [\[CrossRef\]](#)
- Iwata, M.; Kuroda, K.; Hasegawa, Y.; Aoyagi, R.; Maeda, M.; Ishibashi, Y. Phase Transition under Zero-Field Heating after Field Cooling in $(1-x)\text{Pb}(\text{In}_{1/2}\text{Nb}_{1/2})\text{O}_3$ - $x\text{PbTiO}_3$. *Jpn. J. Appl. Phys.* **2009**, *48*, 09KF07. [\[CrossRef\]](#)
- Ishibashi, Y.; Iwata, M. Morphotropic Phase Boundary in Solid Solution Systems of Perovskite-Type Oxide Ferroelectrics. *Jpn. J. Appl. Phys.* **1998**, *37*, L985. [\[CrossRef\]](#)
- Fu, H.; Cohen, R.E. Polarization rotation mechanism for ultrahigh electromechanical response in single-crystal piezoelectrics. *Nature* **2000**, *403*, 281–283. [\[CrossRef\]](#) [\[PubMed\]](#)
- Kutnjak, Z.; Blinc, R.; Ishibashi, Y. Electric field induced critical points and polarization rotations in relaxor ferroelectrics. *Phys. Rev. B* **2007**, *76*, 104102. [\[CrossRef\]](#)
- Viehland, D.; Powers, J. Electromechanical coupling coefficient of $\langle 001 \rangle$ -oriented $\text{Pb}(\text{Mg}_{1/3}\text{Nb}_{2/3})\text{O}_3$ - PbTiO_3 crystals: Stress and temperature independence. *Appl. Phys. Lett.* **2001**, *78*, 3112–3114. [\[CrossRef\]](#)
- Kutnjak, Z.; Petzelt, J.; Blinc, R. The giant electromechanical response in ferroelectric relaxors as a critical phenomenon. *Nature* **2006**, *441*, 956–959. [\[CrossRef\]](#)
- Iwata, M.; Yokoi, R.; Sugiyama, Y.; Maeda, M.; Tachi, Y.; Ishibashi, Y. Temperature-Field Phase Diagrams in $\text{Pb}(\text{Mg}_{1/3}\text{Nb}_{2/3})\text{O}_3$ -29.5% PbTiO_3 . *Ferroelectrics* **2014**, *462*, 19–27. [\[CrossRef\]](#)
- Iwata, M.; Yamashita, K.; Suzuki, S.; Takikawa, Y.; Tachi, Y. Double hysteresis loops and temperature–field phase diagram in $\text{Pb}(\text{Mg}_{1/3}\text{Nb}_{2/3})\text{O}_3$ -29.5% PbTiO_3 . *Jpn. J. Appl. Phys.* **2021**, *60*, SFFA03. [\[CrossRef\]](#)
- Zhao, X.; Wang, J.; Chan, H.L.W.; Choy, C.L.; Luo, H. Effect of a bias field on the dielectric properties of 0.69 $\text{Pb}(\text{Mg}_{1/3}\text{Nb}_{2/3})\text{O}_3$ -0.31 PbTiO_3 single crystals with different orientations. *J. Phys. Condens. Matter* **2003**, *15*, 6899–6908. [\[CrossRef\]](#)
- Zhao, X.; Wang, J.; Peng, Z.; Chan, H.; Choy, C.; Luo, H. Triple-like hysteresis loop and microdomain–macrodomain transformation in the relaxor-based 0.76 $\text{Pb}(\text{Mg}_{1/3}\text{Nb}_{2/3})\text{O}_3$ -0.24 PbTiO_3 single crystal. *Mater. Res. Bull.* **2004**, *39*, 223–230. [\[CrossRef\]](#)
- Iwata, M.; Tamaoki, N.; Arimoto, Y.; Ishibashi, Y. Dielectric tunability in $\text{Pb}(\text{Sc}_{1/2}\text{Ta}_{1/2})\text{O}_3$ single crystals. *Jpn. J. Appl. Phys.* **2017**, *56*, 10PB01. [\[CrossRef\]](#)
- Iwata, M.; Kutnjak, Z.; Ishibashi, Y.; Blinc, R. Theoretical Analysis of the Temperature–Field Phase Diagrams of Perovskite-Type Ferroelectrics. *J. Phys. Soc. Jpn.* **2008**, *77*, 034703. [\[CrossRef\]](#)
- Kaiden, Y.; Iwata, M.; Umeda, Y.; Takikawa, Y.; Tachi, Y. Nonlinear dielectric constant in $\text{Pb}(\text{Mg}_{1/3}\text{Nb}_{2/3})\text{O}_3$ - PbTiO_3 relaxor ferroelectrics. *Jpn. J. Appl. Phys.* **2018**, *57*, 11UC01. [\[CrossRef\]](#)
- Iwata, M.; Saitoh, K.; Kotani, R.; Tagata, S.; Gyobu, K.; Takikawa, Y. Temperature dependence of the aging effect of permittivity in $\text{Pb}(\text{Zn}_{1/3}\text{Nb}_{2/3})\text{O}_3$ - PbTiO_3 and BaTiO_3 single crystals. *Jpn. J. Appl. Phys.* **2023**, *62*, SM1001. [\[CrossRef\]](#)
- Bokov, A.A.; Raevskii, I.P.; Smotrakov, V.G. Influence of ion ordering at lattice sites on the properties of $\text{Pb}2\text{B}'\text{B}''\text{O}_6$ ternary oxides. *Sov. Phys. Solid States* **1983**, *25*, 1168.
- Groves, P. The influence of B-site cation order on the phase transition behaviour of antiferroelectric lead indium niobate. *J. Phys. C Solid State Phys.* **1986**, *19*, 5103–5120. [\[CrossRef\]](#)
- Groves, P. Structural phase transitions and long-range order in ferroelectric perovskite lead indium niobate. *J. Phys. C Solid State Phys.* **1986**, *19*, 111–128. [\[CrossRef\]](#)
- Ohwa, H.; Iwata, M.; Orihara, H.; Yasuda, N.; Ishibashi, Y. Observation of the Distribution of the Transition Temperature in $\text{PbIn}_{1/2}\text{Nb}_{1/2}\text{O}_3$. *J. Phys. Soc. Jpn.* **2000**, *69*, 1533–1537. [\[CrossRef\]](#)
- Yasuda, N.; Ohwa, H.; Kume, M.; Yamashita, Y. Piezoelectric Properties of a High Curie Temperature $\text{Pb}(\text{In}_{1/2}\text{Nb}_{1/2})\text{O}_3$ - PbTiO_3 Binary System Single Crystal near a Morphotropic Phase Boundary. *Jpn. J. Appl. Phys.* **2000**, *39*, L66–L68. [\[CrossRef\]](#)
- Yasuda, N.; Ohwa, H.; Hasegawa, D.; Hayashi, K.; Hosono, Y.; Yamashita, Y.; Iwata, M.; Ishibashi, Y. Temperature dependence of piezoelectric properties of a high Curie Temperature $\text{Pb}(\text{In}_{1/2}\text{Nb}_{1/2})\text{O}_3$ - PbTiO_3 binary system single crystal near a Morphotropic Phase Boundary. *Jpn. J. Appl. Phys.* **2000**, *39*, 5586–5588. [\[CrossRef\]](#)
- Alberta, E.F.; Bhalla, A.S. Piezoelectric properties of $\text{Pb}(\text{InNb})(1/2)\text{O}$ -3- PbTiO_3 solid solution ceramics. *J. Korean Phys. Soc.* **1998**, *32*, S1265–S1267.
- Tu, C.-S.; Chien, R.R.; Hung, C.-M.; Schmidt, V.H.; Wang, F.-T.; Tseng, C.-T. Field-induced orientational percolation to a ferroelectric phase in relaxor $\text{Pb}(\text{In}_{1/2}\text{Nb}_{1/2})1-x\text{Ti}x\text{O}_3$. *Phys. Rev. B* **2007**, *75*, 212101. [\[CrossRef\]](#)
- Zhang, R.; Cao, W. Transformed material coefficients for single-domain 0.67 $\text{Pb}(\text{Mg}_{1/3}\text{Nb}_{2/3})\text{O}_3$ -0.33 PbTiO_3 single crystals under differently defined coordinate systems. *Appl. Phys. Lett.* **2004**, *85*, 6380–6382. [\[CrossRef\]](#)

28. Hosono, Y.; Yamashita, Y.; Sakamoto, H.; Ichinose, N. Dielectric and Piezoelectric Properties of $\text{Pb}(\text{In}_{1/2}\text{Nb}_{1/2})\text{O}_3$ – $\text{Pb}(\text{Mg}_{1/3}\text{Nb}_{2/3})\text{O}_3$ – PbTiO_3 Ternary Ceramic Materials near the Morphotropic Phase Boundary. *Jpn. J. Appl. Phys.* **2003**, *42*, 535–538. [\[CrossRef\]](#)
29. Chen, J.; Li, X.; Zhao, X.; Wang, X.; Chen, C.; Deng, H.; Ren, B.; Jiao, J.; Luo, H. Compositional segregation, structural transformation and property-temperature relationship of high-Curie temperature $\text{Pb}(\text{In}_{1/2}\text{Nb}_{1/2})\text{O}_3$ – $\text{Pb}(\text{Mg}_{1/3}\text{Nb}_{2/3})\text{O}_3$ – PbTiO_3 single crystals. *J. Mater. Sci. Mater. Electron.* **2015**, *26*, 9316–9328. [\[CrossRef\]](#)
30. Lin, D.; Chen, H.; Li, Z.; Xu, Z. Phase diagram and dielectric properties of $\text{Pb}(\text{In}_{1/2}\text{Nb}_{1/2})\text{O}_3$ – $\text{Pb}(\text{Mg}_{1/3}\text{Nb}_{2/3})\text{O}_3$ – PbTiO_3 ceramics. *J. Adv. Dielectr.* **2015**, *5*, 1550014. [\[CrossRef\]](#)
31. Wang, D.; Cao, M.; Zhang, S. Phase diagram and properties of $\text{Pb}(\text{In}_{1/2}\text{Nb}_{1/2})\text{O}_3$ – $\text{Pb}(\text{Mg}_{1/3}\text{Nb}_{2/3})\text{O}_3$ – PbTiO_3 polycrystalline ceramics. *J. Eur. Ceram. Soc.* **2012**, *32*, 433–439. [\[CrossRef\]](#)
32. Zhang, Y.; Li, X.; Liu, D.; Zhang, Q.; Wang, W.; Ren, B.; Lin, D.; Zhao, X.; Luo, H. The compositional segregation, phase structure and properties of $\text{Pb}(\text{In}_{1/2}\text{Nb}_{1/2})\text{O}_3$ – $\text{Pb}(\text{Mg}_{1/3}\text{Nb}_{2/3})\text{O}_3$ – PbTiO_3 single crystal. *J. Cryst. Growth* **2011**, *318*, 890–894. [\[CrossRef\]](#)
33. Zhu, R.; Yang, L.; Fang, B.; Ding, J.; Zhao, X.; Luo, H. Ferroelectric phase transitions of the 0.32PIN-0.345PMN-0.335PT single crystals studied by temperature-dependent Raman spectroscopy, dielectric and ferroelectric performance. *Phase Transit.* **2016**, *90*, 500–508. [\[CrossRef\]](#)
34. Hidayah, N.; Yasuda, N.; Ohwa, H.; Tachi, Y.; Yamashita, Y.; Iwata, M. Poling and Depoling Effects on Dielectric Properties and Domain Structures in Relaxor $24\text{Pb}(\text{In}_{1/2}\text{Nb}_{1/2})\text{O}_3$ – $46\text{Pb}(\text{Mg}_{1/3}\text{Nb}_{2/3})\text{O}_3$ – 30PbTiO_3 near a Morphotropic Phase Boundary Composition. *Jpn. J. Appl. Phys.* **2012**, *51*, 09LC06. [\[CrossRef\]](#)
35. Dul'kin, E.; Kojima, S.; Roth, M. Noncritical behavior in $\text{Pb}(\text{In}_{1/2}\text{Nb}_{1/2})\text{O}_3$ – $\text{Pb}(\text{Mg}_{1/3}\text{Nb}_{2/3})\text{O}_3$ – PbTiO_3 relaxor ferroelectric crystals detected by acoustic emission method. *Ferroelectrics* **2023**, *613*, 12–21. [\[CrossRef\]](#)
36. Wang, Y.; Wang, Z.; Ge, W.; Luo, C.; Li, J.; Viehland, D.; Chen, J.; Luo, H. Temperature-induced and electric-field-induced phase transitions in rhombohedral $\text{Pb}(\text{In}_{1/2}\text{Nb}_{1/2})\text{O}_3$ – $\text{Pb}(\text{Mg}_{1/3}\text{Nb}_{2/3})\text{O}_3$ – PbTiO_3 ternary single crystals. *Phys. Rev. B* **2014**, *90*, 134107. [\[CrossRef\]](#)
37. Wan, Y.; Li, Z.; Ma, M.; Fan, S.; Xu, Z. Temperature and DC Bias Dependences of Dielectric Behavior of Different Oriented 0.23PIN-0.52PMN-0.25PT Single Crystals. *J. Electron. Mater.* **2018**, *47*, 6282–6288. [\[CrossRef\]](#)
38. Wang, Y.; Yuan, G.; Luo, H.; Li, J.; Viehland, D. Phase Transition in the Near-Surface Region of Ternary $\text{Pb}(\text{In}_{1/2}\text{Nb}_{1/2})\text{O}_3$ – $\text{Pb}(\text{Mg}_{1/3}\text{Nb}_{2/3})\text{O}_3$ – PbTiO_3 Relaxor Ferroelectric Crystals. *Phys. Rev. Appl.* **2017**, *8*, 034032. [\[CrossRef\]](#)
39. Lv, P.; Wang, L.; Lynch, C.S. A phenomenological thermodynamic energy function for PIN-PMN-PT relaxor ferroelectric single crystals. *Acta Mater.* **2017**, *137*, 93–102. [\[CrossRef\]](#)
40. Echizenya, K.; Nakamura, K.; Mizuno, K. PMN-PT and PIN-PMN-PT single crystals grown by continuous-feeding Bridgman method. *J. Cryst. Growth* **2019**, *531*, 125364. [\[CrossRef\]](#)
41. Mitsui, T.; Tatsuzaki, I.; Nakamura, E. *An Introduction to the Physics of Ferroelectrics*; Ishibashi, Y.; Tatsuzaki, I.; Nakamura, E.; Burfoot, J.C., Translators; Gordon and Breach: New York, NY, USA, 1976.

Disclaimer/Publisher's Note: The statements, opinions and data contained in all publications are solely those of the individual author(s) and contributor(s) and not of MDPI and/or the editor(s). MDPI and/or the editor(s) disclaim responsibility for any injury to people or property resulting from any ideas, methods, instructions or products referred to in the content.